# Structural characterization and epitope mapping of the AAVX affinity purification ligand

Mario Mietzsch,[1] Manasi Kamat,[2] Kari Basso,[2] Paul Chipman,[1] Juha T. Huiskonen,[3] and Robert McKenna[1]

[1]Department of Biochemistry and Molecular Biology, College of Medicine, Center for Structural Biology, McKnight Brain Institute, University of Florida, Gainesville, FL 32610, USA; [2]Department of Chemistry, Mass Spectrometry Research and Education Center, University of Florida, Gainesville, FL 32610, USA; [3]Institute of Biotechnology, Helsinki Institute of Life Science HiLIFE, University of Helsinki, 00014 Helsinki, Finland

**The application of adeno-associated virus (AAV) vectors in human gene therapies requires reproducible and homogeneous preparations for clinical efficacy and safety. For the AAV production process, often scalable affinity chromatography columns are utilized, such as the POROS CaptureSelect AAVX affinity resin, during downstream processing to ensure highly purified AAV vectors. The AAVX ligand is based on a camelid single-domain antibody capturing a wide range of recombinant AAV capsids. Described here is the identification of the AAV8 capsid epitope to AAVX at 2.3 Å resolution using cryo-electron microscopy. The ligand binds near the 5-fold axis of the capsid in a similar manner to the previously characterized AVB affinity ligand but does not conform to the capsid's icosahedral symmetry. The cross-reactivity of AAVX to other AAV capsids is achieved by primarily interacting with the peptide backbone of the AAV capsid's structurally conserved DE and HI loops. These observations will guide AAV capsid engineering efforts to retain the ability of future recombinant capsid designs to be purified using antibody-based affinity ligands.**

## INTRODUCTION

Adeno-associated virus (AAV) vectors have become the preferred delivery system in the clinic setting for the treatment of a wide variety of monogenetic diseases.[1] Due to the high demand for AAV vectors, with increasing patient numbers and the high doses required, rapid and efficient downstream purification methods are required. Affinity chromatography column methods, utilizing camelid single-domain antibodies (nanobodies) that bind to the surface of the non-enveloped AAV capsids, are often the method of choice.[2] These nanobodies are relatively small (approximately 15 kDa), stable, and possess high affinity and specificity for their antigen.[3] While some of these, such as AVB Sepharose, allow the efficient purification of multiple AAV serotypes,[4] others, such as the POROS CaptureSelect AAV8 or AAV9 affinity ligand, bind specifically to individual AAV serotype capsids.[2] The more recently released AAV-binding resin POROS CaptureSelect AAVX affinity ligand was shown to enable purification of a broad range of divergent AAV capsids, including AAV8 and AAV9.[5] For this pan-AAV-binding property, the affinity ligand needs to bind to highly conserved features on the capsid surface.

The capsid structures of many AAV serotypes have been determined by X-ray crystallography and/or by cryo-electron microscopy (cryo-EM).[6] These studies have shown that the capsids of ∼260 Å diameter possess T = 1 icosahedral symmetry and are composed of 60 viral proteins (VPs). The overall VP structure of the AAVs consists of a conserved β-barrel core with variable surface loops connecting the β strands. Despite significant amino acid sequence variation, the AAVs share similar morphologies, including channels at their 5-fold symmetry axes, protrusions surrounding the 3-fold axes, and depressions at the 2-fold axes. The highest level of surface sequence conservation is observed around the 5-fold channel, which is also the binding site of the AVB affinity ligand.[2]

In this study, the binding site of the AAVX nanobody is determined by cryo-EM to a resolution of 2.3 Å. Similar to AVB, the AAVX nanobody primarily interacts with the DE and HI loops around the 5-fold axis but binds in a non-icosahedral mode, possibly mediated by alternative side-chain conformations of asparagine (N) 670. The capsid-AAVX interaction information is critical for capsid engineering efforts to retain the purification ability of novel AAV vectors.
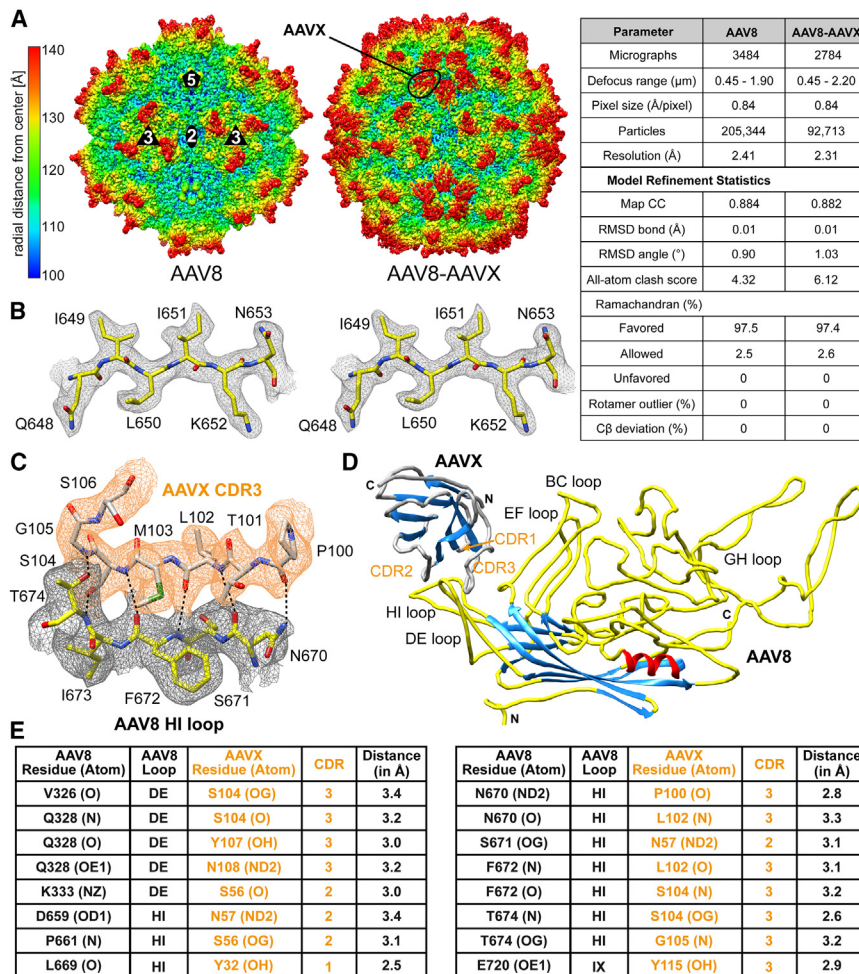
## RESULTS

The three-dimensional (3D) image reconstruction with icosahedral averaging of cryo-EM data collected on AAV8 capsids alone and in complex with AAVX resulted in density maps of 2.4 and 2.3 Å resolution, respectively (Figure 1A). The AAV8 capsid structure of this study is, as expected, identical to the previously determined AAV8 capsid structures with $C_\alpha$ root-mean-square deviation (RMSD) values <0.4 Å.[7,8] The AAVX-AAV8 complex map exhibited five distinct densities for AAVX surrounding the 5-fold axis that were absent in the AAV8 alone map. This matches the results shown by

**Figure 1. Determination of the AAVX interaction to AAV capsids**

(A) The 3D reconstruction maps of AAV8 and the AAV8:AAVX complex are shown down a 2-fold axis. The maps are colored according to the radial distance from the capsid center, as indicated by the scale bar. The positions of the icosahedral 2-, 3-, and 5-fold axes are shown on the AAV8 capsid map. The location of a single AAVX molecule is indicated on the AAV8:AAVX map. (B) Amino acid residues modeled into each map for the βH strand are shown. The amino acid residues are shown in stick representation and colored according to atom type: C, yellow; O, red; and N, blue. The cryo-EM reconstruction parameters and model refinement statistics are provided to the right. (C) The modeled HI loops of AAV8 and CDR3 of AAVX are shown inside the cryo-EM map. Hydrogen bonding between AAV8 and AAVX is indicated by black dashed lines. (D) The AAV8 VP (yellow) is shown with the bound AAVX (gray) as ribbon/coil diagrams, with the β strands in blue and the α helix in red. The N and C termini, the surface, and CDRs are labeled. (E) All contacts between AAV8 and AAVX via hydrogen bonding are listed, providing the residue numbers, contacting atoms, loop location, and distance between the atoms in Å.

the AAV8 HI loop, which adopted a different rotamer conformation in the presence ("on") or absence ("off") of AAVX (Figure 2D).

The binding location of AAVX is reminiscent of the interaction of the previously determined complex of AAV8 with the AVB nanobody.[2] Similar to AAVX, AVB binds around the 5-fold axis but, unlike AAVX, appears to interact with the capsid in an icosahedral fashion, as density for the nanobody is still observed at higher σ levels (Figure 3A). In fact, fitting of the atomic AAVX model into the AVB density showed that both nanobodies nearly perfectly overlap with a $C_\alpha$ RMSD of ∼0.4 Å (Figure 3B). Furthermore, most of the amino acid side chains in the CDRs appeared to be identical with a few exceptions (e.g., H59Y or T101S; Figure 3C), indicating that both nanobodies may have a common origin.

ThermoFisher.[9] The high-resolution data enabled reliable modeling of the AAV8 capsid and the majority of the AAVX nanobody, allowing the identification of the contact residues (Figures 1B and 1C), with the AAVX primarily interacting with the DE and HI loops of the AAV8 capsid with its complementarity-determining region (CDR) 2 and CDR3 loops (Figures 1D and 1E). A total of 16 potential hydrogen bond interactions (<3.5 Å) per nanobody to the AAV8 capsid were observed.

Analysis of the icosahedrally averaged map showed that the density of AAVX was weaker than the corresponding capsid and not visible at higher sigma (σ) thresholds, indicating a lower occupancy of the nanobody (Figure 2A). Thus, a localized reconstruction of the 5-fold region with symmetry relaxation was conducted, revealing that in the map determined to 3.3 Å resolution and in all defined 3D classes during the reconstruction, only two adjacent-bound nanobodies per 5-fold were bound (Figures 2B and S2). The modeled AAV8 and AAVX residues built into the icosahedral map (Figure 1D) fitted the localized map without further adjustments (Figure 2C). The only exception was asparagine 670 of

## DISCUSSION

The AAV-specific affinity ligands allow rapid purification of AAV vectors.[10] However, as the number of engineered AAV variants for gene delivery applications increases,[11] the capsid-binding interfaces of these purification ligands need to be characterized to ensure compatibility to guide capsid engineering efforts. Previously, the binding sites of the AVB and the AAV8 and AAV9 CaptureSelect affinity ligands have been mapped.[2] The development of the latter two ligands was necessary because AVB did not allow the purification of AAV9 or did so only with poor efficiency, in the case of AAV8.[2,4] In contrast, AAVX enabled the purification of the vast
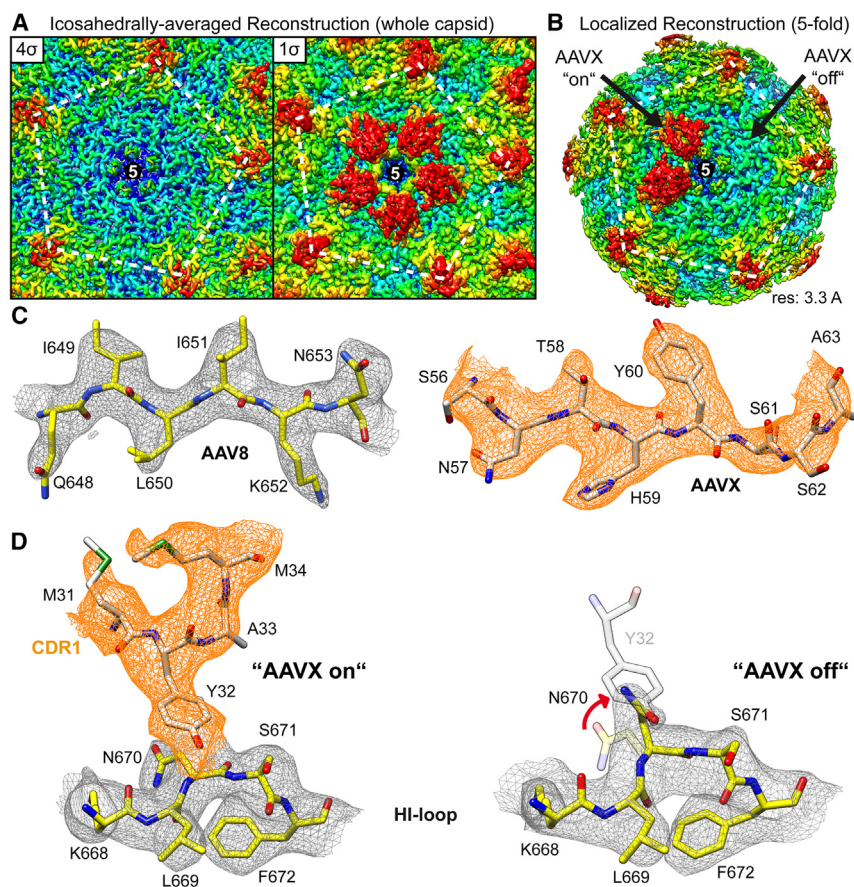
**Figure 2. The asymmetric binding of AAVX**

(A) The icosahedral-averaged density map of the AAV8:AAVX complex is shown at a sigma (σ) threshold of 4 and 1, centered down a 5-fold axis. The position of the 5-fold axis is indicated and a pentagon connecting the surrounding 3-fold protrusions added to the map. (B) A density map of the 5-fold region is shown after localized reconstruction of the region. (C) Amino acid residues of the AAV8 βH strand (left) are displayed inside the localized-reconstructed map. To the right, residues of AAVX are shown in the same map. (D) The modeled AAV8 HI-loop residues in the presence or absence of AAVX are shown inside the localized-reconstructed map.

the symmetry of the capsid. Additional symmetry mismatches arise when viruses interact with receptors,[15] antibodies,[16] and/or other proteins resulting in structural rearrangements but also when the capsid packages eject their genetic material.[17] In the AAV8 map, in the absence of AAVX, N670 adopts the AAVX-off conformation, indicating that AAVX binding may induce the rotamer change of the asparagine side chain. However, why this change occurs only in two neighboring VP monomers at the 5-fold region is unclear. Future studies may further characterize the stoichiometry of AAVX and AVB binding to the AAV capsids by mass photometry, analytical ultracentrifugation, or charge detection mass spectrometry (CDMS).[18–21] Nonetheless, the "reduced" binding of AAVX (using only two for the available five sites) is clearly sufficient for AAV vector purification.

majority of AAV capsid variants.[5] Despite these differences, AAVX is nearly structurally indistinguishable from AVB in the high-resolution cryo-EM maps. In the absence of the amino acid sequence for the AVB nanobody, only a few potential sequence differences are identifiable. Other substitutions could be present but may not be distinguishable due to amino acids with similar-sized side chains. This similarity may indicate that AAVX was developed based on AVB to confer the ability to purify a wide range of AAV capsids. The identified AAVX contacts to AAV8 showed that the nanobody primarily interacts with the peptide backbone of the capsid. The side chain interactions to K333 and E720 are likely not critical since these amino acids are not conserved in other purifiable AAV serotypes (Figure S1).[5] As a result, the AAVX nanobody likely binds similarly to most AAVs, as shown for AAV1 (Figure S1), as long as the loop conformation of the DE and HI loops is maintained and long-chained amino acids are not introduced to the capsid that interfere with AAVX binding, as seen for N670 (Figure 2D). The binding characteristics of AAVX to the 5-fold region highlight the notion that the AAV capsids are not perfect icosahedrons. Non-conforming T = 1 attributes of "icosahedral capsids" have been previously suggested.[12–14] In the case of the AAVs, the lower incorporation of VP1 and VP2 with their highly flexible N termini compared to VP3 and the packaged genome cannot conform to

## MATERIALS AND METHODS

### Cryo-EM sample preparation, data collection, and processing

AAVX-purified AAV8 capsids produced in HEK293 cells[7] were mixed with the CaptureSelect Biotin Anti-AAVX Conjugate (ThermoFisher) in an excess of affinity ligands compared to the capsid (120 nanobodies per capsid) and vitrified using a Vitrobot Mark 4 (ThermoFisher). Cryo-EM data for these grids were collected at the UMASS-Chan CryoEM Core using a Titan Krios electron microscope operated at 300 kV. The data collection parameters are provided in Figure 1. MotionCor2 was used to align the raw movie frames with dose weighting.[22] The motion-corrected micrographs were imported into cisTEM[23] for icosahedral 3D reconstruction. Scipion was utilized for the localized reconstruction of the 5-fold region[24] (for details, see the supplemental materials and methods). All the atomic models were built and refined in Coot and PHENIX.[25,26]

### AAVX sequencing

To determine the amino acid sequence of AAVX, 8 μg of the AAVX-biotin conjugate were digested with sequencing-grade trypsin (Promega) using the manufacturer's recommended protocol. Briefly,
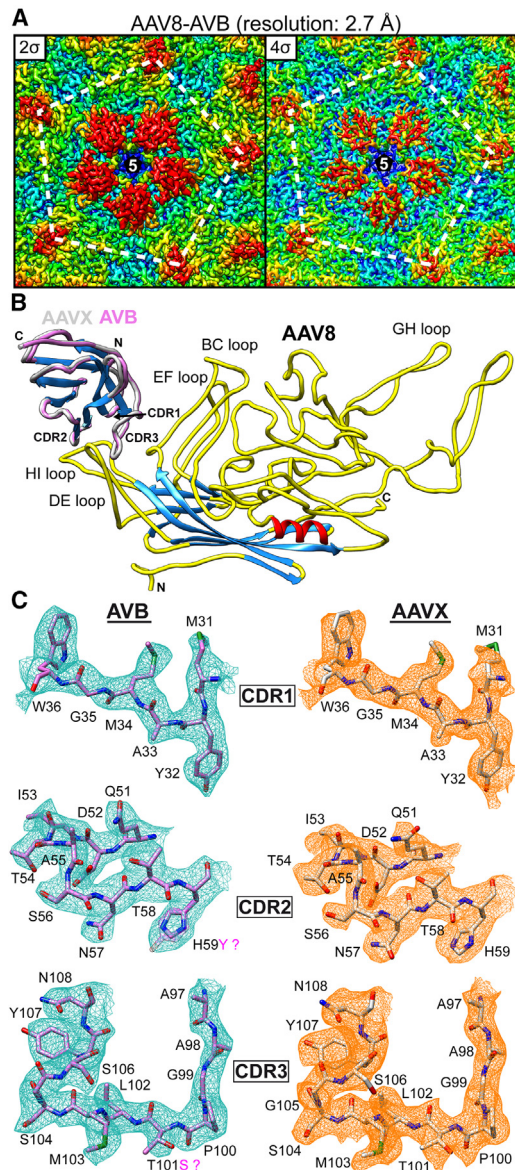
**Figure 3. Comparison of the AVB and AAVX affinity ligands**

(A) The density map of the AAV8:AVB complex is shown at 2- and 4σ centered onto the 5-fold axis. (B) Superposition of the AVB and AAVX affinity ligands bound to AAV8 shown as ribbon/coil diagrams. (C) The modeled AAVX CDRs are shown inside the AVB (blue mesh) and AAVX (orange mesh) density map. The amino acid residues are shown in stick representation and colored according to atom type: C, orchid/gray; O, red; N, blue; and S, green.

samples were reduced by adding 1 μL of 0.1 M dithiothreitol in 100 mM ammonium bicarbonate for 30 min at 56°C, followed by alkylation with 0.54 μL of 55 mM iodoacetamide in 100 mM ammonium bicarbonate for 30 min at room temperature in the dark. Enzymatic digestion was performed using 1 μL of freshly made trypsin (1 μg/μL) by incubating at 37°C for 2 h. The enzyme activity was inhibited by the addition of 0.5% TFA. The mass spectrometry (MS)

analysis was immediately performed to ensure high-quality tryptic peptides with minimal non-specific cleavage. Proteomics analysis of the digested protein samples was performed using nano-liquid chromatography tandem MS (nano-LC/MS/MS) (supplemental materials and methods). The data were imported into the Peaks AB 3.0 software (Bioinformatics Solution) for automated protein *de novo* sequencing.

## DATA AND CODE AVAILABILITY

The AAV8 and AAV8-AAVX cryo-EM reconstructed density maps and models built were deposited in the Electron Microscopy Data Bank (EMDB) with the accession numbers EMDB: EMD-46740, PDB: 9DC2 (AAV8 alone), and EMDB: EMD-46741, PDB: 9DC3 (AAV8-AAVX).

## AUTHOR CONTRIBUTIONS

Conceptualization, M.M. and R.M.; investigation, M.M., M.K., K.B., and P.C.; writing – original draft, M.M.; writing – review & editing, M.M., M.K., K.B., P.C., J.T.H., and R.M.; supervision, M.M. and R.M. All authors read and approved the final manuscript.

## DECLARATION OF INTERESTS

J.T.H. is co-founder and CEO of Nanometria, a limited liability company.

## SUPPLEMENTAL INFORMATION

Supplemental information can be found online at https://doi.org/10.1016/j.omtm.2024.101377.

## REFERENCES

1. Zhao, Z., Anselmo, A.C., and Mitragotri, S. (2022). Viral vector-based gene therapies in the clinic. Bioeng. Transl. Med. 7, e10258. https://doi.org/10.1002/btm2.10258.

2. Mietzsch, M., Smith, J.K., Yu, J.C., Banala, V., Emmanuel, S.N., Jose, A., Chipman, P., Bhattacharya, N., McKenna, R., and Agbandje-McKenna, M. (2020). Characterization of AAV-Specific Affinity Ligands: Consequences for Vector Purification and Development Strategies. Mol. Ther. Methods Clin. Dev. 19, 362–373. https://doi.org/10.1016/j.omtm.2020.10.001.

3. Tang, H., Gao, Y., and Han, J. (2023). Application Progress of the Single Domain Antibody in Medicine. Int. J. Mol. Sci. 24, 4176. https://doi.org/10.3390/ijms24044176.

4. Wang, Q., Lock, M., Prongay, A.J., Alvira, M.R., Petkov, B., and Wilson, J.M. (2015). Identification of an adeno-associated virus binding epitope for AVB sepharose affinity resin. Mol. Ther. Methods. Clin. Dev. 2, 15040. https://doi.org/10.1038/mtm.2015.40.

5. Florea, M., Nicolaou, F., Pacouret, S., Zinn, E.M., Sanmiguel, J., Andres-Mateos, E., Unzu, C., Wagers, A.J., and Vandenberghe, L.H. (2023). High-efficiency purification of divergent AAV serotypes using AAVX affinity chromatography. Mol. Ther. Methods. Clin. Dev. 28, 146–159. https://doi.org/10.1016/j.omtm.2022.12.009.

6. Mietzsch, M., Jose, A., Chipman, P., Bhattacharya, N., Daneshparvar, N., McKenna, R., and Agbandje-McKenna, M. (2021). Completion of the AAV Structural Atlas: Serotype Capsid Structures Reveals Clade-Specific Features. Viruses 13, 101. https://doi.org/10.3390/v13010101.

7. Mietzsch, M., Barnes, C., Hull, J.A., Chipman, P., Xie, J., Bhattacharya, N., Sousa, D., McKenna, R., Gao, G., and Agbandje-McKenna, M. (2020). Comparative Analysis of the Capsid Structures of AAVrh.10, AAVrh.39, and AAV8. J. Virol. 94, e01769-19. https://doi.org/10.1128/JVI.01769-19.

8. Nam, H.J., Lane, M.D., Padron, E., Gurda, B., McKenna, R., Kohlbrenner, E., Aslanidi, G., Byrne, B., Muzyczka, N., Zolotukhin, S., and Agbandje-McKenna, M. (2007). Structure of adeno-associated virus serotype 8, a gene therapy vector. J. Virol. *81*, 12260–12271. https://doi.org/10.1128/JVI.01304-07.

9. Drulyte, I., Raaijmakers, H., Hermans, P., Adams, H., and Radajainia, M. (2022). Cryo-EM Structure of AAV8 and Epitope Mapping of CaptureSelect AAVX (ThermoFisher note).

10. Smith, R.H., Levy, J.R., and Kotin, R.M. (2009). A simplified baculovirus-AAV expression vector system coupled with one-step affinity purification yields high-titer rAAV stocks from insect cells. Mol. Ther. *17*, 1888–1896. https://doi.org/10.1038/mt.2009.128.

11. Li, C., and Samulski, R.J. (2020). Engineering adeno-associated virus vectors for gene therapy. Nat. Rev. Genet. *21*, 255–272. https://doi.org/10.1038/s41576-019-0205-4.

12. Parent, K.N., Schrad, J.R., and Cingolani, G. (2018). Breaking Symmetry in Viral Icosahedral Capsids as Seen through the Lenses of X-ray Crystallography and Cryo-Electron Microscopy. Viruses *10*, 67. https://doi.org/10.3390/v10020067.

13. Stass, R., Ilca, S.L., and Huiskonen, J.T. (2018). Beyond structures of highly symmetric purified viral capsids by cryo-EM. Curr. Opin. Struct. Biol. *52*, 25–31. https://doi.org/10.1016/j.sbi.2018.07.011.

14. Wang, J.C.Y., Mukhopadhyay, S., and Zlotnick, A. (2018). Geometric Defects and Icosahedral Viruses. Viruses *10*, 25. https://doi.org/10.3390/v10010025.

15. Zhang, R., Liu, Y., Yu, F., Xu, G., Li, L., Li, B., and Lou, Z. (2024). Structural basis of the recognition of adeno-associated virus by the neurological system-related receptor carbonic anhydrase IV. PLoS Pathog. *20*, e1011953. https://doi.org/10.1371/journal.ppat.1011953.

16. Mietzsch, M., Nelson, A.R., Hsi, J., Zachary, J., Potts, L., Chipman, P., Ghanem, M., Khandekar, N., Alexander, I.E., Logan, G.J., et al. (2024). Structural characterization of antibody-responses from Zolgensma treatment provides the blueprint for the engineering of an AAV capsid suitable for redosing. Preprint at bioRxiv. https://doi.org/10.1101/2024.05.01.590489.

17. Gliwa, K., Hull, J., Kansol, A., Zembrzuski, V., Lakshmanan, R., Mietzsch, M., Chipman, P., Bennett, A., and McKenna, R. (2024). Biophysical and Structural Insights into AAV Genome Ejection. J. Virol.

18. Mietzsch, M., Liu, W., Ma, K., Bennett, A., Nelson, A.R., Gliwa, K., Chipman, P., Fu, X., Bechler, S., McKenna, R., and Viner, R. (2023). Production and characterization of an AAV1-VP3-only capsid: An analytical benchmark standard. Mol. Ther. Methods Clin. Dev. *29*, 460–472. https://doi.org/10.1016/j.omtm.2023.05.002.

19. Yarawsky, A.E., Ciatto, C., Slade, P., Figueroa, N., Burgner, J.W., DeLion, M., and Paul, L.N. (2024). Quantitation of AAV in a dual-vector system using SV-AUC. J. Pharmaceut. Sci. https://doi.org/10.1016/j.xphs.2024.10.049.

20. Nakatsuka, R., Yamaguchi, Y., Hirohata, K., Shimojo, S., Murakami, M., Rocafort, M.A.V., Tsunaka, Y., Fukuhara, M., Torisu, T., and Uchiyama, S. (2024). Multimass Analysis of Adeno-Associated Virus Vectors by Orbitrap-Based Charge Detection Mass Spectrometry. Anal. Chem. *96*, 17037–17046. https://doi.org/10.1021/acs.analchem.4c05229.

21. Wagner, C., Fuchsberger, F.F., Innthaler, B., Lemmerer, M., and Birner-Gruenberger, R. (2023). Quantification of Empty, Partially Filled and Full Adeno-Associated Virus Vectors Using Mass Photometry. Int. J. Mol. Sci. *24*, 11033. https://doi.org/10.3390/ijms241311033.

22. Zheng, S.Q., Palovcak, E., Armache, J.P., Verba, K.A., Cheng, Y., and Agard, D.A. (2017). MotionCor2: anisotropic correction of beam-induced motion for improved cryo-electron microscopy. Nat. Methods *14*, 331–332. https://doi.org/10.1038/nmeth.4193.

23. Grant, T., Rohou, A., and Grigorieff, N. (2018). cisTEM, user-friendly software for single-particle image processing. Elife *7*, e35383. https://doi.org/10.7554/eLife.35383.

24. Abrishami, V., Ilca, S.L., Gomez-Blanco, J., Rissanen, I., de la Rosa-Trevín, J.M., Reddy, V.S., Carazo, J.M., and Huiskonen, J.T. (2021). Localized reconstruction in Scipion expedites the analysis of symmetry mismatches in cryo-EM data. Prog. Biophys. Mol. Biol. *160*, 43–52. https://doi.org/10.1016/j.pbiomolbio.2020.05.004.

25. Emsley, P., and Cowtan, K. (2004). Coot: model-building tools for molecular graphics. Acta Crystallogr. D Biol. Crystallogr. *60*, 2126–2132. https://doi.org/10.1107/s0907444904019158.

26. Adams, P.D., Afonine, P.V., Bunkóczi, G., Chen, V.B., Davis, I.W., Echols, N., Headd, J.J., Hung, L.W., Kapral, G.J., Grosse-Kunstleve, R.W., et al. (2010). PHENIX: a comprehensive Python-based system for macromolecular structure solution. Acta Crystallogr. D Biol. Crystallogr. *66*, 213–221. https://doi.org/10.1107/s0907444909052925.